

SCIENTIFIC REPORTS



Correction: Author Correction

OPEN

Methane utilization in *Methylobacterium alcaliphilum* 20Z^R: a systems approach

Ilya R. Akberdin^{1,2}, Merlin Thompson¹, Richard Hamilton¹, Nalini Desai³, Danny Alexander³, Calvin A. Henard⁴, Michael T. Guarnieri⁴ & Marina G. Kalyuzhnaya¹

Biological methane utilization, one of the main sinks of the greenhouse gas in nature, represents an attractive platform for production of fuels and value-added chemicals. Despite the progress made in our understanding of the individual parts of methane utilization, our knowledge of how the whole-cell metabolic network is organized and coordinated is limited. Attractive growth and methane-conversion rates, a complete and expert-annotated genome sequence, as well as large enzymatic, ¹³C-labeling, and transcriptomic datasets make *Methylobacterium alcaliphilum* 20Z^R an exceptional model system for investigating methane utilization networks. Here we present a comprehensive metabolic framework of methane and methanol utilization in *M. alcaliphilum* 20Z^R. A set of novel metabolic reactions governing carbon distribution across central pathways in methanotrophic bacteria was predicted by *in-silico* simulations and confirmed by global non-targeted metabolomics and enzymatic evidences. Our data highlight the importance of substitution of ATP-linked steps with PPI-dependent reactions and support the presence of a carbon shunt from acetyl-CoA to the pentose-phosphate pathway and highly branched TCA cycle. The diverged TCA reactions promote balance between anabolic reactions and redox demands. The computational framework of C₁-metabolism in methanotrophic bacteria can represent an efficient tool for metabolic engineering or ecosystem modeling.

Climate change concerns linked to increasing concentrations of anthropogenic methane have spiked interest in biological methane utilization as a novel platform for improving ecological and human well-being^{1–4}. Methane-utilizing microbes (i.e., methanotrophs) are becoming an attractive and efficient microbial platform for organic manufacturing of renewable fuels and chemicals^{3–6}. Recent application of modern metabolic engineering tools has furthered methane-based biotechnology, leading to construction of novel biocatalyst traits with great biotechnological potential^{7–9}. The recent progress in this area has also highlighted the need for a deeper understanding of the methane-conversion network organization.

Our knowledge of aerobic methane utilization is founded on a number of remarkable discoveries in the biochemistry, physiology, genetics, and ecology of this unique biological function in Proteobacteria^{10–12}. The established network of methane utilization has been revisited through the discovery of high redundancy of core functional oxidation machinery and the incredible flexibility of the redox balancing pathways^{13–20}. Access to complete genome sequences of methanotrophic bacteria^{21,22} enables whole-genome metabolic reconstruction and flux-balance modeling^{23–25}. Several limitations of the top-down modeling of methylotrophy have been highlighted²⁴, including limited knowledge of redox transfer reactions, flexibility of the primary methane oxidation pathways, and lack of data on energy maintenance. Herein, we applied a set of systems-level approaches for comprehensive investigation of the methane utilization network in *Methylobacterium alcaliphilum* 20Z^R (a rifampicin-resistant derivative of the strain 20Z^{14–16}). Complete and expert-annotated genomic information, a large set of genetic tools, wide-ranging enzymatic studies, and the availability of whole-genome transcriptomic data make 20Z^R an ideal model system for understanding the central metabolic pathways associated with methane oxidation^{16,26–34}. *M. alcaliphilum* 20Z^R possesses only particulate methane monooxygenase (pMMO) for the first step of methane conversion. The enzyme is a mixed function oxidase, in which one atom from O₂

¹Biology Department and Viral Information Institute, San Diego State University, San Diego, USA. ²Institute of Cytology and Genetics and Novosibirsk State University, Novosibirsk, Russia. ³Metabolon, Inc. 617 Davis Drive, Suite 400, Durham, NC, 27713, USA. ⁴National Bioenergy Center, National Renewable Energy Laboratory, 15013 Denver West Parkway, MS 3323, Golden, CO, 80401, United States. Correspondence and requests for materials should be addressed to M.G.K. (email: mkalyuzhnaya@mail.sdsu.edu)

goes to methanol and the other to water, requiring the input of 2 electrons and 2 protons. To date the source of electrons is still unknown. The second step of the methane oxidation pathway is catalyzed by a periplasmic pyrroloquinoline quinone-linked methanol dehydrogenase. Two enzymes are predicted, a Ca-dependent MxaFI system and La-dependent XoxF¹⁵. Genome annotation for the strain 20Z predicts multiple pathways for formaldehyde oxidation, including tetrahydromethanopterin- and tetrahydrofolate-linked pathways, formaldehyde dehydrogenase, and the oxidative ribulose monophosphate cycle¹⁵. The genome has two clusters encoding NAD-dependent formate dehydrogenases: 1) NAD-linked, tungsten (W)-dependent formate dehydrogenase; and 2) a partial NAD-linked, molybdenum-dependent formate dehydrogenase. Only the first system is expressed under methane-growth conditions, even if W is not supplied. Since formate is typically accumulated in the growth media^{16,33}, it could be suggested, that the enzyme is only partially active. The impact of tungsten addition on growth of *Methylomicrobium alcaliphilum* 20Z^R has never been evaluated. Genome annotation indicates that metabolic pathways for carbon assimilation are highly branched and include the assimilatory ribulose monophosphate pathway (RuMP) and the partial serine cycle¹⁶. Two variants of the RuMP have been described in 20Z¹⁶. Furthermore, it has been demonstrated that 75% of intercellular pyruvate comes from the pyrophosphate (PPi)-mediated Embden-Meyerhof-Parnas pathway (EMP); and 25% from the Entner–Doudoroff pathway (EDD)¹⁶. Furthermore, more recent evidence suggested the presence of the phosphoketolase pathway, which has been proposed to contribute to acetyl-CoA production³⁵. The genomic data predict a complete TCA cycle¹⁵. At least three possible pathways for 2-oxoglutarate to succinyl-Co-A/succinate conversion could be identified: 1) the traditional 2-oxoglutarate dehydrogenase complex; 2) 2-oxoglutarate:ferredoxin oxidoreductase; and 3) γ -aminobutyric acid shunt³⁶. However, the exact arrangement of the TCA in the methanotroph remains to be established. Furthermore, while the functional significance of the PPi-phosphofructokinase, a key enzyme of the EMP has been well established, the role of other PPi-dependent enzymes involved in central metabolism and anaplerotic CO₂ fixation has never been evaluated. In this study, we focus on mathematical modeling of methane and methanol utilization pathways in 20Z^R taking into account updated metabolic networks, optimized growth parameters (growth rate and biomass yields), methane/oxygen consumption, and as well as enzymatic and global non-targeted metabolomics data.

Results and Discussion

Growth optimization: impact of microminerals. It could be predicted, that the growth of the *M. alcaliphilum* 20Z^R will depend on availability of Cu, Ca (or La) and W. The *M. alcaliphilum* 20Z^R does not grow without copper, and the optimal growth is observed between 5–10 μ M of Cu (II) (data not shown). As tungsten is not a standard component of methanotrophic growth media, a set of batch cultivation experiments with/without tungsten (W) was performed to examine its effects on growth and formate excretion. The growth rate of the culture did not change, however the final biomass yield increased by $7.5 \pm 2.5\%$. Concentrations of C₁–C₄ organic acids in the growth medium were measured using NMR as described previously¹⁶. We found that formate production in cells grown in the presence of tungsten is reduced significantly, suggesting that tungsten limitation is a major factor contributing to formate excretion (Table 1). The data confirmed that NAD-linked, tungsten-dependent formate dehydrogenase is the main enzyme predicted for formate oxidation in *M. alcaliphilum* 20Z^R. Therefore, all experiments carried-out in this work, were done with the W-supplemented growth medium. The substitution of Ca with La in the medium trace solution induced significant shifts in central metabolic pathways, which will be described elsewhere. In this study, we present data collected upon growth with calcium, i.e., with the Ca-dependent MDH, linked to cytochrome c_L.

Biomass composition. Overall biomass of *M. alcaliphilum* 20Z^R cells consists of $44.9 \pm 2.6\%$ carbon (C), $8.1 \pm 2.4\%$ nitrogen (N) and 6.8 ± 0.1 hydrogen (H). The composition of main precursors (amino acids, fatty acids, nucleic acids, carbohydrates) was measured and summarized in Table 2. The main components were estimated as follows: $43 \pm 2\%$ amino acids, $14 \pm 1\%$ lipids, $9.7 \pm 3.6\%$ RNA, $8.1 \pm 1.4\%$ glycogen, $4 \pm 0.3\%$ DNA, $1.5 \pm 0.1\%$ ectoine, and $0.9 \pm 0.2\%$ sucrose. The list of intracellular metabolites, concentrations of cytochromes, ATP and PPi, phospholipids were compiled from published literature^{16,25,26,37}.

Flux balance model and growth parameters. The model consists of three compartments (extracellular space, periplasm and cytoplasm) and 396 internal enzymatic reactions (represented by 407 genes), 16 transport reactions between cell compartments, 422 metabolites and 20 exchange rates for nutrients and excreted compounds (see Supplemental Material, Table S1).

Since the energetics of methane oxidation in 20Z^R can be linked to aerobic or anaerobic respiration and fermentation, electron transfers were further refined by incorporating aerobic respiration pathways (from NADH/H⁺, FADH₂, and cytochrome c_L), anaerobic respiratory pathways, and fermentation pathways¹⁶. As the source of electrons is still unknown, we incorporated a pMMO-specific electron carrier (e-donor), which could be reduced via three pathways: 1) a ubiquinone (UQH₂)/e-carrier to represent UQ-linked methane oxidation; 2) a cytochrome c_L (cyt_L)/e-carrier to represent direct coupling between pMMO and methanol dehydrogenase; and 3) cyt_L and cyt_bc1/2e-carriers to represent previously proposed reverse (also known as uphill) electron transfer^{18,24}. The electron transfer reactions were connected to the production of proton/ion motive force (PMF), with the following ratios: electron transfer from NADH/H⁺ to ubiquinone linked to the transfer of 4 H⁺ (or 0.4 PMF); electron transfer from ubiquinol to cytochrome bc1 (cyt_bc1) and to cytochrome c (cyt_c) linked to the transfer of 4 H⁺ (or 0.4 PMF); electron transfer from cytochrome c (cyt_c) or from cytochrome c_L (cyt_L) to cytochrome oxidase linked to the transfer of 2 H⁺ (or 0.2 PMF). The electron transfer from ubiquinol to ubiquinol oxidases was also linked to the translocation of 4 H⁺ (or 0.4 PMF). ATP production via oxidative phosphorylation was set as the following: 1 ATP produced per 3 H⁺ translocated. The initial value of non-growth and growth-associated ATP maintenance were adapted from *Methylomicrobium buryatense* 5 G(B1)²⁴.

Compound	%	SD	mmol/g DCW biomass	Organism source	Reference
Amino Acids	43	2			
Alanine			0.366	<i>M. alcaliphilum</i> 20Z	This study
Arginine			0.149	“	“
Asparagine			0.119	“	“
Aspartate			0.409	“	“
Cysteine			0.024	“	“
Glutamate			0.487	“	“
Glutamine			0.15	“	“
Histidine			0.078	“	“
Glycine			0.339	“	“
Isoleucine			0.203	“	“
Leucine			0.332	“	“
Lysine			0.182	“	“
Methionine			0.093	“	“
Phenylalanine			0.171	“	“
Proline			0.161	“	“
Serine			0.194	“	“
Threonine			0.229	“	“
Tryptophan			0.072	“	“
Tyrosine			0.111	“	“
Valine			0.278	“	“
Ectoine	1.5	0.1	0.106	“	“
Lipids	14	1			
FAME (8.8%)					
C14 (myristate)			0.010	<i>M. alcaliphilum</i> 20Z	“
C15 (pentadecylic acid)			0.002	“	“
C16 (palmitate)			0.329	“	“
C18 (stearate)			0.002	“	“
Phosphatidylserine (1%)*			0.002	“	26
Phosphatidylethanolamine (50%)*			0.086	“	“
Dipalmitoyl phosphatidate (4)*			0.007	“	“
Cardiolipin (11)*			0.019	“	“
Phosphatidylglycerol (34)*			0.059	“	“
Sterols and bacteriohopanepolyol	0.02				
tetrahymanol			0.025	<i>M. alcaliphilum</i> 20Z	59
aminotriol (III), 65% of BHP			0.008	“	60
3-Me-aminotriol, 31% BHP			0.003	“	“
aminotetrol and 3-Me-aminotetrol, <3% BHP			“	“	0.001
Intracellular metabolites	1.5	—			
Ribulose-5-phosphate/Ribose-5-phosphate			0.001	<i>M. alcaliphilum</i> 20Z	16
Fructose-1, 6-bisphosphate			0.001	“	“
Fructose-6-phosphate			0.003	“	“
Glucose-6-phosphate			0.002	“	“
Glyceraldehyde-3-phosphate/Dihydroxyacetone			0.003	“	“
6-Phosphogluconic acid			0.00015	“	“
2-dehydro-3-deoxy-phosphogluconate			0.000003	“	“
Phosphoglycerate			0.006	“	“
Phosphoenolpyruvate			0.005	“	“
Pyruvate			0.015	“	“
Acetyl-CoA			0.0001	“	“
Succinate			0.002	“	“
Malate			0.004	“	“
Fumarate			0.001	“	“
Citrate			0.001	“	“
Glycerate			0.001	“	“
ATP			0.005	<i>Methylomonas methanica</i>	61
Continued					

Compound	%	SD	mmol/g DCW biomass	Organism source	Reference
ADP			0.002	<i>M. extorquens</i> AM1	62
AMP			0.001	<i>M. extorquens</i> AM1	-"
NAD			0.002	<i>M. extorquens</i> AM1	-"
NADH			0.002	<i>M. extorquens</i> AM1	-"
NADP			0.001	<i>M. extorquens</i> AM1	-"
NADPH			0.001	<i>M. extorquens</i> AM1	-"
polyP (PPi)			0.029	<i>Methylomonas methanica</i>	61
Cofactors					
Cytochrome c			0.00036	<i>M. alcaliphilum</i> 20Z	37
B12			0.00000063	-"	63
Ubiquinol-8			0.00022	Assumption	62
Protoheme			0.00022	Assumption	-"
coenzyme-A			0.00022	Assumption	-"
FMN			0.00022	Assumption	-"
FMNH2			0.00022	Assumption	-"
FAD			0.00022	Assumption	-"
SAM			0.00022	Assumption	-"
Glutathione			0.00022	Assumption	-"
Carbohydrates	1.38	0.2			
Mannose			0.002	<i>M. alcaliphilum</i> 20Z	64
Ramnose			0.0002	-"	-"
Glycogen	8.1	1.4	0.448	-"	This study
Sucrose	0.9	0.2	0.026	-"	65
Ribose			0.036	-"	64
Maltose			0.008	-"	-"
Arabinose			0.022	-"	-"
Galactose			0.005	-"	-"
Cell wall					
Peptidoglycan	9.1	-	0.053	Assumed as in <i>M. buryatense</i> 5GB1	24
LPS (lipid IVA and KDO)	0.027	-	0.002	-"	-"
RNA	9.7	3.6			This study
ATP			0.050	<i>M. alcaliphilum</i> 20Z	-"
UTP			0.050	-"	-"
CTP			0.047	-"	-"
GTP			0.047	-"	-"
DNA	4.0	0.28			This study
dATP			0.0021	<i>M. alcaliphilum</i> 20Z	-"
dTTP			0.0021	-"	-"
dCTP			0.0020	-"	-"
dGTP			0.0020	-"	-"
Ash	5			Assumed as in <i>M. buryatense</i> 5GB1	40
BIOMASS (measured)	98.2	8.8			
3-PG (balance)	1.8		0.010		
TOTAL	100.0				
ELEMENTAL COMPOSITION					
C	44.9	2.6		<i>M. alcaliphilum</i> 20Z	This study
N	8.1	2.4		-"	-"
H	6.8	0.1		-"	-"
EXCREATED PRODUCTS					
Formate			0.7	<i>M. alcaliphilum</i> 20Z	-"
Acetate			0.02	-"	-"
Lactate			0.004	-"	-"
EPS	0.5-1%		1%	-"	-"
DCW (% WCW)	25 ± 3.4				
Growth parameters					
Continued					

Compound	%	SD	mmol/g DCW biomass	Organism source	Reference
Continuous culture (5% CH₄: 5%O₂:N₂ balance)					
Methane Uptake (mmol g CDW ⁻¹ h ⁻¹)	11.7 ± 0.14				This study
Oxygen Uptake (mmol g CDW ⁻¹ h ⁻¹)	14.7 ± 0.9				- ^a -
O ₂ /CH ₄ Uptake Ratio	1.25 ± 0.06				- ^a -
CO ₂ production (mmol g CDW ⁻¹ h ⁻¹)*	0.37 ± 0.05				- ^a -
Specific Growth Rate (h ⁻¹)	0.12 ± 0.01				- ^a -
Batch culture (10% CH₄:Air)					
Methane Uptake (mmol g CDW ⁻¹ h ⁻¹)	18.6 ± 1.4				This study
Oxygen Uptake (mmol g CDW ⁻¹ h ⁻¹)	24.4 ± 2.1				- ^a -
O ₂ :CH ₄ Uptake Ratio	1.31 ± 0.07				- ^a -
Specific Growth Rate (h ⁻¹)	0.14 ± 0.02				- ^a -

Table 1. Biomass composition and growth parameters of *Methylobacterium alcaliphilum* 20Z^R. *CO₂ production rates are below expected due to high pH of the growth medium.

Compound	-Na ₂ WO ₄	+Na ₂ WO ₄
Formate	45.8 ± 1.3	2.4 ± 0.9
Acetate	2.4 ± 0.2	2.0 ± 0.1
Lactate	ND	trace
Succinate	ND	trace
Pyruvate	ND	ND
Citrate	ND	ND

Table 2. Accumulation of excreted organic acids (mg g⁻¹ DCW) by *M.alcaliphilum* 20Z^R grown in batch culture with or without sodium tungsten (0.07 mg L⁻¹).

Additional constraints were added as follows: 1) only water and CO₂ are included as the expected excretion products; excreted formate, acetate, lactate, and exopolysaccharides were incorporated as part of the biomass equation and included in the biomass flux; 2) the methane consumption rate was set at 11.7 ± 0.14 mmol g⁻¹ DCW h⁻¹, (DCW, dry cell weight) based on measurements taken during continuous culture growth (at observed $\mu = 0.12 \pm 0.01$ h⁻¹); and 3) the oxygen consumption rate was set at >11.7 and <20.6 mmol gDCW⁻¹ h⁻¹. The lowest parameter of oxygen consumption is based on the stoichiometry of methane oxidation, as 1 mol of oxygen is needed for oxidation of 1 mol methane. The upper limit represents the highest oxygen consumption rate observed during methane-limited growth (unpublished data). The oxygen consumption rate during exponential growth in continuous culture was 14.7 ± 0.9 mmol g⁻¹ DCW h⁻¹.

The initial metabolic model was further refined using enzymatic data (compiled in Table 3), and published ¹³C-carbon-labeling analyses, and transcriptomic data¹⁶. A number of central metabolic pathway reactions, including a set of reactions for the anaplerotic carbon fixation and PPI-linked reactions²⁹ were validated and the following modifications were made: 1) both oxaloacetate and malate were set as key entry points for CO₂ fixation, via pyruvate carboxykinase (PC, EC 6.4.1.1) or PP_i-phosphoenolpyruvate carboxykinase (PEPCK, EC 4.1.1.38) and malic enzyme reactions (ME, EC 1.1.1.40), respectively; 2) interconversions between pyruvate and phosphoenolpyruvate were via pyruvate kinase (PYK, EC 2.7.1.40) and pyruvate phosphate dikinase (PPDK; EC 2.7.9.1); (3) all variants of the RuMP and the serine cycle were incorporated into the model;^{24,35} (4) all possible variants of the TCA cycle were included^{15,36}.

An overview of the central metabolic pathways is shown in Fig. 1 (a detailed figure is provided as supplemental Figure S1). We ran a set of *in silico* flux balance analysis (FBA) experiments using the COBRA toolbox to validate the stoichiometric completeness of the proposed metabolic network at all steps of the model development. Simulations for unconstrained network supported the direct coupling (electrons for methane oxidation comes from cytC_L) as the most optimal solution for methane oxidation, however the predicted O₂/CH₄ consumption was low (Table 4). As could be predicted, incorporation of PPI-reactions slightly improved biomass yield. An additional constraint on intracellular source of PPI, with biosynthesis reactions as the only source, lead to the reduction of biomass and an increase in O₂ consumption. However, even after the modification, the predictions differ from experimental measurements (Table 4). Specifically, the predicted growth rate was higher (0.145 vs 0.12), while predicted O₂:CH₄ consumption rate was low (1.21 vs 1.26). Two possible explanations were explored further: 1) ATP maintenance in methanotrophic bacteria is higher than assumed³⁸; and 2) ubiquinol (UQH₂) serve as supplemental sources of electrons for methane oxidation. The ATP requirements in methane grown cells of *M. alcaliphilum* 20Z^R were measured, and the contribution of UQH₂ was investigated by further constraining metabolic networks to observed oxygen consumption rate.

ATP maintenance requirement in *M. alcaliphilum* 20Z^R. Methane-limitation experiments were carried out, in order to estimate non-growth-associated ATP maintenance³⁹. Cells of 20Z^R were supplied with

Enzyme	Cofactor	Enzyme activity (or Vmax) nmol min ⁻¹ mg protein ⁻¹	Km/Ks (mM)	References
Methane monooxygenase (pMMO)	whole cells assay	120 ± 40		64
Methanol dehydrogenase	PMS/Ca	230 ± 10		-“-
Formate dehydrogenase	NAD ⁺	132 ± 7		-“-
NADH-dehydrogenase (with 100 mM NaCl)	NADH	454 ± 50		37
NADH-dehydrogenase (without NaCl)	NADH	383 ± 80		-“-
ATPase	ADP	8.6 ± 0.4		-“-
Hydroxypyruvate reductase*	NADPH	41 ± 2		66
	NADH	26 ± 7		-“-
Serine-glyoxylate aminotransferase,		ND		64
Glucokinase*	ATP	217 ± 8	0.32	67
3-Hexulose phosphate synthase*	Ru5P	172 ± 9	0.13	68
Phosphoglucose isomerase		32 ± 2		-“-
6-Phosphofructokinase*	F6P/PPi	577 ± 60	0.64	30
	F6P/ATP	ND		-“-
	FBP/PPi	805 ± 80	0.095	-“-
Glucose-6-phosphate dehydrogenase	NAD ⁺	23 ± 2		64
	NADP ⁺	34 ± 2		-“-
6-Phosphogluconate dehydrogenase	NADP ⁺	32 ± 2		-“-
	NAD ⁺	12 ± 1		-“-
Fructose-1,6-bisphosphate aldolase		35 ± 2		64
KDPG aldolase		62 ± 3		-“-
Enolase		10 ± 1		-“-
Fructokinase			2.5	69
Acetate kinase*	ADP	1290 ± 31	5.6	31
Phosphoketolase methane methanol	TPP	0.11 ± 0.02 0.047 ± 0.009		This study
Pyruvate dehydrogenase methane methanol	NAD ⁺	120 ± 20 290 ± 44		-“-
2-Oxoglutarate dehydrogenase	NAD ⁺	N.D.		-“-
Succinate semialdehyde dehydrogenase	NADP	80 ± 17.4		-“-
Glutamate decarboxylase	NAD ⁺	7.4 ± 1.1		-“-
Pyruvate kinase*	ADP	200 ± 12*		16
Citrate synthase		6 ± 0.5		64
Isocitrate dehydrogenase	NAD ⁺	ND		-“-
	NADP ⁺	11 ± 1		-“-
Malate dehydrogenase*	Malate (NAD ⁺)	1500 ± 150	0.11 (0.45)	32
	Oxaloacetate (NADH)	2100 ± 200	0.34 (0.025)	-“-
Malate lyase	ATP, CoA	ND		64
Glutamate dehydrogenase	NADH	4 ± 0.5		-“-
	NADPH	3 ± 0.2		-“-
Alanine dehydrogenase	NADPH	ND		-“-
	NADH	2 ± 0.1		-“-
Glutamate synthase	NADPH	14 ± 1		-“-
Glutamine synthetase	Mn ²⁺ , ATP	204 ± 10		-“-

Table 3. Summary of kinetic parameters for enzymes from central metabolic pathways in *M.alcaliphilum* 20Z^R. *Purified enzyme.

various concentrations of methane from 0 to 2 mmol and the growth rate and methane consumption rate were measured. We found that 20Z^R cells require 3.6 ± 0.3 mmol CH₄ gDCW⁻¹ h⁻¹ to sustain metabolic activity but not grow. Methane concentrations below this parameter led to decreases in cell density, while higher methane concentrations supported cell growth. Using the assumed ATP yield $Y_{ATP, max} = 6$ mol ATP per one mol CH₄ consumed, the non-growth-associated ATP requirement was calculated as 21.6 mmol ATP g DCW⁻¹ hr⁻¹.

Growth-associated ATP maintenance for 20Z^R was found by fitting the reconstructed model to the experimentally determined biomass yield. We plotted the CH₄-uptake rate against the growth rate from continuous culture experiments (Table 1). Model simulations were carried out for various values of growth-associated ATP maintenance and the range of 90–110 mmol ATP g DCW⁻¹ was found to match experimental data (Fig. 2 see Methods).

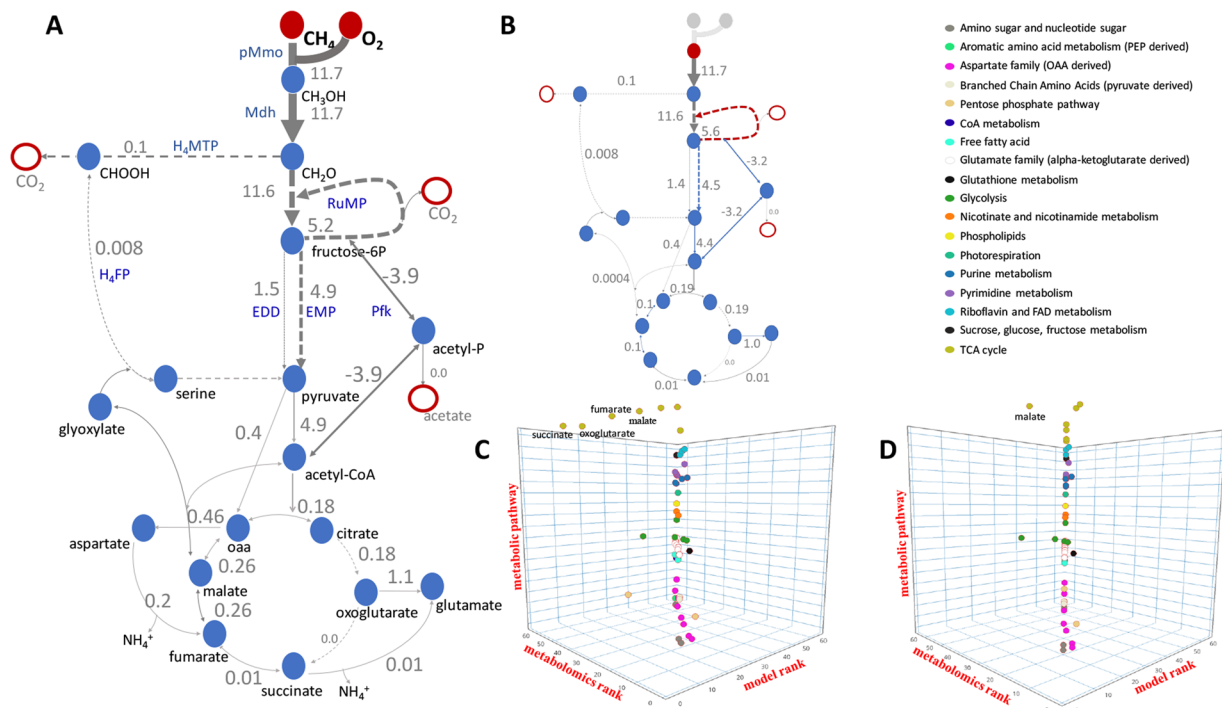


Figure 1. Central metabolic pathways of methane (A) and methanol (B) utilization in *Methylobacterium alcaliphilum* 20Z^R and results of FBA analyses. Red circles indicate input substrates (CH₄, O₂, or CH₃OH), White circles with red outlines indicate excreted compounds (CO₂ and acetate); thickness of arrow represents predicted value of the corresponding flux via the reaction (solid arrow) or metabolic pathway (dotted arrows); (C,D) 3D plots of comparative analysis of metabolic profiling versus predicted flux ratios between the same growth conditions (axis X – model rank; axis Y – metabolomics rank; axis Z – metabolic pathway that a compound belongs to). (C) Comparison of results for complete TCA cycle (Spearman's index equals to 0.9, p-value = 2.7E-24); (D) Comparisons of results for branched TCA cycle and reverse phosphoketolase reaction (R = 0.99, p-value = 2E-55).

Network	O ₂ :CH ₄	CO ₂ production (mmol g CDW ⁻¹ h ⁻¹)	growth rate (h ⁻¹)
Source of electrons			
Cytochrome c _L	1.2	5.2	0.146
Ubiquinol	1.50	7.7	0.09
Initial network*	1.2	5.2	0.146
CO ₂ fixation via PEPC	1.2	5.2	0.147
PPi-reactions (PFK, PEPC, PPD, PPi-ase)	1.19	5.1	0.149
Biosynthesis as a sole source of PPi (without PPiase)	1.21	5.3	0.145
Reversible PPK	1.18	5.1	0.15
Branched TCA	1.18	5.1	0.15
Fermentation mode (without ATPase)	1.02	1.5	0.06
Final network O₂-input constrained**	1.26	5.7	0.136
Experimental data	1.26–1.31	-	0.12–0.14

Table 4. *In silico* predictions for different metabolic arrangements of methane utilization. *Methane uptake is set to 11.7 mmol g CDW⁻¹h⁻¹; **Oxygen uptake is set to 14.7 mmol g CDW⁻¹h⁻¹.

While the updated maintenance coefficients improved the correlation between simulations and observed experimental data, the oxygen consumption rates were still below expected 1.26.

Model predictions depending on simultaneous constraints of O₂ and CH₄ consumption. A set of additional *in-silico* simulations with constrained methane and oxygen consumption rates was carried out in order to investigate correlations between biomass production and O₂/CH₄ ratios (Fig. 3). The optimal solution for biomass production directly correlated with oxygen consumption, reaching the optimal output at 1.2–1.4—supporting direct coupling as the most compelling model for the observed O₂:CH₄ consumption ratio of 1.26. The contribution of electron transfer from NADH (via UQH₂) gradually increased, ranging from 30% at a O₂:CH₄

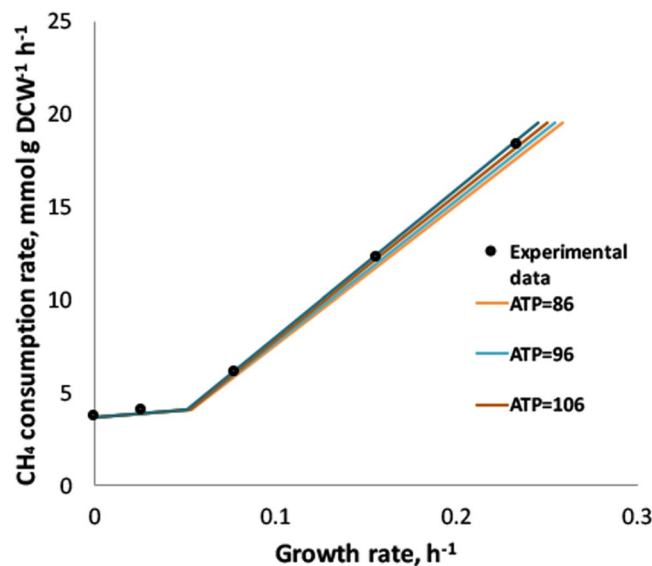


Figure 2. Experimentally measured (dots) and predicted growth rates for different CH_4 consumption rates at different level of ATP maintenance. Axis X: values of growth rate (h^{-1}); Axis Y: CH_4 consumption rates ($\text{mmol g DCW}^{-1} \text{h}^{-1}$).

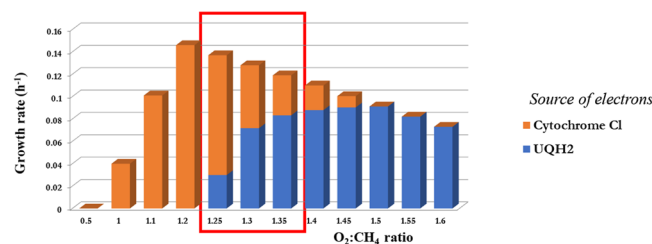


Figure 3. Contribution of different sources of redox for methane utilization depending on $\text{O}_2:\text{CH}_4$ ratio. The height of the colored bar reflects the biomass production or percentage of the carbon flux a specific electron donor proportionally to 100% biomass at the particular value of $\text{O}_2:\text{CH}_4$ ratio.

consumption ratio of 1.3 to 75% at a O_2/CH_4 consumption ratio of 1.4, and completely replaced direct coupling at a $\text{O}_2:\text{CH}_4$ consumption ratio of 1.5. The switch to the redox arm leads to a decrease in biomass production. As the majority of the experimental data lay in the range of 1.25–1.4, optimal biomass production could not be modeled by any single mode, whether it was UQ-mediated or direct coupling. In summary, the most realistic behavior of the system could be modeled by dual simultaneous constraints on oxygen and methane consumption.

To further validate this prediction, we estimated the parameters for growth at low oxygen tension. It has been shown that upon oxygen limitation the strain switches to a fermentation mode¹⁶. We ran an initial unconstrained model with only a constraint on oxygen uptake (O_2 consumption rate was set to $12 \text{ mmol gDCW}^{-1} \text{h}^{-1}$, or $\text{O}_2/\text{CH}_4 = 1.02$). This modification resulted in significantly reduced bacterial growth (0.06 h^{-1}) and an extremely elevated excretion of acetate ($3.83 \text{ mmol gDCW}^{-1} \text{h}^{-1}$). According to the *in-silico* simulations, the phosphoketolase pathway is the most compelling mode of methane fermentation, with the majority of cellular ATP produced from an acetate kinase reaction. Both the growth rate and the increase in acetate excretion have been previously observed as main outcomes of O_2 -limiting growth^{16,40}. Furthermore, the kinetic properties of purified acetate kinase from *M. alcaliphilum* 20Z support the *in-silico* prediction (Table 3³¹).

Model validation: metabolomics data. The validity of the metabolic model was further assessed by metabolomics. Metabolomic profiles were obtained for cells grown in continuous culture on methane, as well as for exponentially grown cells from batch cultures on methane and methanol. Two hundred and fifty-three compounds were identified in bacterial cell pellets. The complete list of the non-targeted metabolites is presented in Table S2 (Supplemental materials).

We conducted statistical comparisons between methane-grown cells (methane batch or optimal culture considered as control) and methanol culture condition to reveal key differences in metabolic signatures (summarized in Table S3). When compared to growth on methane, the most noticeable changes in cells grown on methanol were the increase of glycine (5.7-fold), aspartate (3.7-fold), glutamine (3.1-fold), glucose (4.8-fold), fructose (2.1-fold), and intermediates of fatty acid degradation (i.e., 3-hydroxydecanoate, 47-fold), while the intracellular levels of the TCA Krebs cycle intermediates (citrate, aconitate, malate, fumarate) and phosphosugars (fructose

6-phosphate, hexose diphosphates, sedoheptulose-7-phosphate), pyruvate and acetylphosphate were reduced. Cells grown at low oxygen tension showed metabolite patterns similar to those observed previously, and had elevated levels of fatty acids [i.e., 10-heptadecenoate (17:1n7)], lactate, and succinate¹⁶.

The magnitude of changes between the two groups was compared to flux changes between the same two conditions predicted by the model. A positive and statistically significant correlation between predicted fluxes and experimental metabolomics data was observed. For example, the model predicts an increased carbon flux into the pool of amino acids under methanol growth, and a slight drop of the RuMP cycle. These predictions correspond to the directions of changes for metabolites in these pathways measured by biochemical profiling. Calculations of Spearman's index, which is proper to use in the presence of a small number of observations, between these data sets have confirmed the statistically significant correlations between model predictions and experimental measurements (Fig. 1C,D).

The comparison also highlighted a set of metabolites whose changes contradict the model predictions, including intermediates of the TCA cycle, pentose phosphate pathway, and pyruvate (Fig. 1C). Additional modifications of the model and *in-silico* simulations were carried out. Changing the phosphoketolase reaction directionality (from fructose 6-phosphate → acetylphosphate + erythrose 4-phosphate to acetylphosphate + glyceraldehyde phosphate → xylulose 5-phosphate) improved model predictions for intermediates of the pentose phosphate pathway. We also considered a complete TCA cycle for methanol and methane growth, which reduced the Spearman's index between metabolomics profiling and flux ratios to 0.9 (p-value = 2.7E-24). Simulations with a complete TCA cycle for methanol growth and an incomplete (knockout of 2-oxoglutarate dehydrogenase) TCA cycle for methane growth led to the Spearman's index of 0.94 (p-value = 1.1E-30). However, changes in fumarate and succinate levels did not correlate with predicted flux changes, so the metabolic reactions producing or consuming those compounds were investigated further. Simulations with an unusual TCA cycle⁴¹—in which oxoglutarate is converted to glutamate and then to succinate via succinate-semialdehyde dehydrogenase and glutamate carboxylase—and, additionally, oxaloacetate converted to aspartate and then to fumarate via aminotransferase and aspartate lyase resulted in the Spearman's index of 0.99 (p-value = 2E-55).

Finally, a set of enzymatic analyses were set up to validate the updated metabolic network. The activity of phosphoketolase was measured in actively grown 20Z^R cells demonstrating that the pathway is active upon growth on methane and methanol (Table 3); however, the highest activity of phosphoketolase is found in methane-grown cells. We also detected relatively high activity of succinate-semialdehyde dehydrogenase, supporting the hypothesis of a branched TCA cycle at the oxoglutarate node.

Concluding Remarks

Here we demonstrated the applicability of the systems approach to analyze and improve our understanding of the methane utilization network in *M. alcaliphilum* 20Z^R. A genome-scale metabolic model of *M. alcaliphilum* 20Z^R was constructed and refined using continuous cell culture parameters.

The flux balance analysis of the metabolic model quantified initial steps of methane oxidation, RuMP cycle, EMP/EDD pathways, TCA cycle; major routes for nucleotide, amino acid, and lipid biosynthesis, and fatty acid metabolism; as well as biomass growth under different conditions of the strain cultivation.

The model analysis has also identified the crucial role of an additional constraint on the O₂ consumption rate. Due to the high plasticity of the redox reactions in the strain, the additional constraint on O₂-input helped the model to navigate across the metabolic network and correctly reproduce experimentally observed parameters (growth rate and corresponding yields), and thus make accurate predictions.

Furthermore, we show that the integration of non-targeted metabolomics data with metabolic flux predictions can help to refine the central metabolic pathways, by highlighting nodes poorly resolved by *in-silico* reconstruction. The model simulations suggest that PPI-dependent reactions in the central metabolic pathways might contribute to energy preservation upon oxygen limitation, as well as improve carbon conversion efficiency. Global, non-targeted, metabolomic profiling combined with *in-silico* simulations uncovered a set of highly interconnected nodes at the level of acetyl-CoA, fumarate, and glutamate. Further enzymatic studies confirmed the carbon flux from acetyl-CoA to xylulose-5-phosphate via phosphoketolase, from glutamate to succinate via succinate-semialdehyde dehydrogenase and glutamate carboxylase, and from aspartate to fumarate via aspartate lyase. The model will serve to inform hypothesis-driven strain engineering strategies, targeting enhanced methane conversion rate and efficiency.

Methods

Metabolic modeling. To build the metabolic framework for 20Z^R we used the whole genome sequence of *Methylomicrobium alcaliphilum* 20Z (NC_016112.1)¹⁵ and the previously published metabolic reconstruction for the closely related species, *Methylomicrobium buryatense* 5G(B1)²⁴. Each reaction in these metabolic pathways was checked for mass and charge balances except reactions coupled with electron transfer system. The model was developed in a format compatible for FBA^{42–44}. Moreover, to standardize reaction and metabolite IDs in our model according to BiGG Models ID Specification and Guidelines⁴⁵, we used iAF692 model data⁴⁶ for almost all of entities and KEGG abbreviations for enzymatic reactions, for which we could not find corresponding BiGG reactions. To link genes with reactions, the NCBI Reference Sequence annotation, NC_016112.1, was applied. To mathematically model the methane utilization network and to solve FBA optimization problems we employed GNU Linear Programming Kit (GLPK) (<http://www.gnu.org/software/glpk/>) solver in MATLAB using the well-known COBRA toolbox designed for flux balance model reconstruction and analyses⁴⁷. To visualize metabolic networks and obtained fluxes we employed the Escher web-tool (Figure S1⁴⁸).

Strain and growth media. *M. alcaliphilum* 20Z^R cells were grown using modified P media (g/L): KNO₃, 1; MgSO₄ × 7H₂O, 0.2; CaCl₂ × 2H₂O, 0.02; NaCl, 30; trace solution, 1 ml/L of trace solution⁹; and supplemented with

20 ml/L of phosphate solution (5.44 g KH_2PO_4 ; 5.68 g Na_2HPO_4) and 20 ml/L of 1 M carbonate buffer. The following methane mixtures were used for bioreactor studies: (i) 5% CH_4 : 3.5% O_2 to represent oxygen-limiting conditions; (ii) 5% CH_4 : 5% O_2 , to represent optimal growth; and (iii) 2.5% CH_4 : 10% O_2 to represent methane-limiting conditions. Methane mixtures were directly purged into bioreactor culture at 0.1 sL h^{-1} rate. In batch cultures, methane (99.9%, Airgas) was injected into vials to represent 10–20% of the headspace. For methanol growth cultures were supplemented with 0.5% methanol.

Cultivation. Culturing was carried out in either closed vials (50 ml cultures in 250 ml vials, or 200 ml cultures in 1 L bottles) with shaking at 200 r.p.m. or bioreactor cultures (fed-batch or turbidostat). Two types of bioreactors were used: 1) a DASbox mini bioreactor (0.5 L working volume; 200 ml culture) with two individual bioreactor units, each having automatic temperature, pH, and DO controls, a sample port for measuring OD, and a coupling to a BlueSens sensor system for simultaneous measuring off-gases (CH_4 , O_2 , and CO_2); or 2) a 2.7 L bench top BioFlo 110 modular bioreactor (New Brunswick Scientific, Edison, NJ, USA).

Batch cultures were grown in 125 ml, 250 ml, or 1.2 L bottles. The headspace:medium was set at 4:1 ratio. CH_4 , O_2 , and CO_2 composition of the headspace were determined using an SRI GC system. Control set of samples include only uninoculated media. The methane and oxygen consumption and CO_2 production rates were calculated by estimating decline (or increase) of the corresponding compounds over time. The data were analyzed to assess yield (Y), growth rate, and O_2 /substrate ratios. In addition, samples (15 ml) were taken for metabolomics.

ATP maintenance experiments. To estimate growth-dependent and non-growth associated ATP maintenance cells of $20Z^R$ were pre-grown to $\text{OD} = 0.36 \pm 0.05$ and transferred to new vials supplemented with various amounts of methane added to headspace (0, 0.02, 0.04, 0.08, 0.1, 0.2, 0.4, 0.8, 1.6 mmol). Each experiment was represented by 3–6 biological replicates. Vials with cultures were placed back onto shaking platform. OD and CH_4 , O_2 and CO_2 composition were measured every 30 min – 1 h over 12 hours. The growth rates of methanotrophic bacteria correlated with the initial concentrations of substrate added. No growth was observed in cultures supplemented with methane below $3.6 \text{ mmol g}^{-1} \text{ DCW h}^{-1}$.

Methane utilization for maintenance and growth is mathematically expressed as:

$$q_{\text{CH}_4} = m_{\text{CH}_4} + \frac{\mu}{Y_{\text{max}}}$$

where m_{CH_4} is the methane requirement for non-growth-associated maintenance activities, Y_{max} is the maximum biomass yield including growth-associated maintenance, and μ is the growth rate³⁹. These ATP requirements were determined from a plot of methane uptake versus optimal computed growth rate, given the experimentally determined values for m_{CH_4} and Y_{max} . m_{CH_4} has been observed to have value equals to $3.6 \text{ mmol CH}_4 \text{ g DCW}^{-1} \text{ h}^{-1}$, while Y_{max} has a value $0.6 \text{ g DCW per g of CH}_4$. Using the assumed ATP yield $Y_{\text{ATP,max}} = 6 \text{ mol ATP per one mol CH}_4 \text{ consumed}$ and the y-intercept ($3.6 \text{ mmol CH}_4 \text{ g DCW}^{-1} \text{ hr}^{-1}$), the non-growth-associated ATP requirement was calculated as $21.6 \text{ mmol ATP g DCW}^{-1} \text{ hr}^{-1}$. To estimate growth-associated ATP maintenance the model was simulated by varying only the CH_4 consumption rate upon different values of growth-associated ATP maintenance as a stoichiometric coefficient in the biomass equation ('BOF' in Supplemental Material, Table S1). Figure 2B demonstrates agreement between the equation and the flux balance approach and the corresponding growth-associated ATP requirement is the range of 90–110 mmol ATP g DCW⁻¹.

Dry cell weight measurement. Cultures (150 ml) from bioreactors were centrifuged to collect the biomass. After careful removal of the liquid phase, tubes of known weight with biomass were weighed (to obtain wet-cell biomass weight), lyophilized overnight using a Labconco freeze-dry system and weighed again. The observed DCW parameters were as follows: 1 L of cell culture with $\text{OD} = 1$ corresponds to $0.336 \pm 0.025 \text{ g DCW}$.

Biomass composition. Samples of lyophilized biomass were submitted to AminoAcids (aminoacids.com) for complete amino acid analysis, and to Matrix Genetics (Seattle, WA, <http://matrixgenetics.com>) for FAME derivatization and GC-MS analysis. The intracellular concentration of glycogen was determined using anthron reagent⁴⁹; ectoine concentration was determined using an HPLC assay⁵⁰. For glycogen measurements $20Z^R$ biomass (dry) was lysed by incubation of with potassium hydroxide (10% KOH) at 95 °C for 1 h. After neutralization and centrifugation (14000 rpm @ 15 min, 4 °C), ethanol was added to the supernatants (two volumes) and samples were refrigerated overnight. The precipitated glycogen was resuspended in 1 ml of DI H₂O and centrifuged again (14000 rpm, 15 min, 4 °C). 1 ml of 0.2% (w/v) anthrone reagent (95% sulfuric acid) was added to 0.2 ml resuspended glycogen and incubated for 15 minutes, after which the sample was measured using a Janeway 632OD spectrophotometer and 620 nm. The concentrations of glycogen were estimated by comparing to glycogen standards prepared in the same manner as cell samples. Extracellular polysaccharides were measured in samples of broth using a sulfuric acid assay⁵¹. Extracellular concentrations of formate, acetate, and lactate were measured as previously described¹⁶.

Non-targeted metabolite profiling. Metabolomic analysis of cells and spent supernatant from cultures of the *M. alcaliphilum* $20Z^R$ was performed using Metabolon's untargeted global biochemical profiling platform [<http://www.metabolon.com/technology.aspx>] and according to the published protocol⁵². The data represent accurate relative quantification only for individual compounds across all the samples which contain it. The original scale data represent raw ion counts for the integrated peaks specifically representing each compound. The scaled data is generated by simply dividing each value for a compound by the median (among detected samples), then imputing any null values with the minimum detected value. Thus, the scaled data are centered around 1.0 (median) for all compounds, but the variation among the samples is not affected^{53,54}. Statistical analyses were performed on natural log-transformed data.

Statistical comparison between predicted flux changes and biochemical profiling. Statistical comparison between methane-grown cells (methane batch) and methanol culture condition was initially conducted to reveal key differences in metabolic signatures. The magnitudes of changes between two groups were compared to predicted flux changes between the same two conditions. An enzymatic reaction with the highest value of flux for biosynthesis of corresponding metabolite was used to calculate flux ratio between two growth conditions. In order to estimate Spearman's correlation index, predicted flux ratios and metabolic signatures were ranked according to the method⁵⁵. 3D plots reflected metabolomics and model ranks taking into account metabolic pathways for measured substances were generated with assistance of Plotly tool (Plotly Technologies Inc. Collaborative data science. Montréal, QC, 2015; <https://plot.ly>).

Isolation of soluble protein fraction. Cell lysates were generated from biomass cultivated under above described conditions. Cells were pelleted via centrifugation for 1 min at 13,000 g and culture supernatants were discarded. Cell pellets were quenched in liquid nitrogen, thawed and solubilized on ice in 1 mL of lysis buffer (50 mM MOPS, pH 7.4, 50 mM NaCl, supplemented with 1X cOmplete Protease Inhibitor Cocktail solution (Roche Diagnostics Corporation, Indianapolis, IN)). The cells were then sonicated on ice at 4 °C, at 90% power setting for 30 seconds \times 3 cycles, with a one minute cool-down period between sonication cycles using a Braun-Sonic-L ultrasonicator. Lysates were cleared via centrifugation at 16,000 \times g at 4 °C for 5 minutes, and the supernatants were isolated for use in subsequent enzymatic analysis.

Enzyme activity determination. Cell lysates were generated from biomass cultivated under above described conditions. Cells were pelleted via centrifugation for 1 min at 13,000 g and culture supernatants were discarded. Cell pellets were quenched in liquid nitrogen, thawed and solubilized on ice in 1 mL of lysis buffer (50 mM MOPS, pH 7.4, 50 mM NaCl, supplemented with 1X cOmplete Protease Inhibitor Cocktail solution (Roche Diagnostics Corporation, Indianapolis, IN)). The cells were then sonicated on ice at 4 °C, at 90% power setting for 30 seconds \times 3 cycles, with a one minute cool-down period between sonication cycles using a Braun-Sonic-L ultrasonicator. Lysates were cleared via centrifugation at 16,000 g at 4 °C for 5 minutes, and the supernatants were isolated for use in subsequent enzymatic analysis.

Enzymatic assays for pyruvate dehydrogenase (PDH), alpha ketoglutarate dehydrogenase (AKGDH), succinate semialdehyde dehydrogenase (SSADH), and glutamate carboxylase (GC) were conducted using methodology adapted from⁵⁶. Briefly, enzymatic activity was quantitated via continuous spectrophotometric rate determination at 340 nm following enzyme incubation with substrate, Coenzyme A, and beta-nicotinamide adenine dinucleotide (or oxidized nicotinamide adenine dinucleotide for SSADH) at 30 °C. Final assay reaction concentrations for PDH, AKGDH, and GC were as follows: 50.8 mM MOPS, 0.2 mM MgCl₂, 0.01 mM CaCl₂, 0.3 mM cocarboxylase (thiamine pyrophosphate), 0.12 mM coenzyme A, 2.0 mM beta-nicotinamide adenine dinucleotide, 2.6 mM L-cysteine, 5 mM substrate, and 25ug total protein. Final reaction concentrations for SSADH were as follows: 87 mM potassium pyrophosphate, 3 mM 2-mercaptoethanol, 1.3 mM β -nicotinamide adenine dinucleotide phosphate, 5.0 mM succinic semialdehyde, 0.83% (v/v) glycerol, 2.5 mM potassium phosphate, and 25ug total protein.

Phosphoketolase activity was measured using a hydroxamate assay that detects acetyl phosphate^{35,57,58}. Briefly, 100 μ L reactions in reaction buffer [30 mM potassium phosphate (pH 6.5), L- cysteine hydrochloride (2 mM), sodium fluoride (20 mM), sodium iodoacetate (10 mM), thiamine pyrophosphate (1 mM), and fructose 6-phosphate (30 mM) (Sigma)] were initiated by the addition of 25 μ g total protein. Reactions were incubated at 37 °C for 1 h. After incubation, 50 μ L of 2 M hydroxylamine hydrochloride (pH 7.0) was added to the reaction and incubated at room temperature for 10 min. Reactions were then terminated by adding 300 μ L of a 1:1 mixture of 2.5% ferric chloride in 2 M hydrochloric acid and 10% trichloroacetic acid. A color change due to ferric-hydroxamate formation was measured at A505nm, and the concentration of acetyl-P formed during the initial reaction was calculated by regression analysis compared to known standards.

All absorbance measurements were conducted using a FLUOstar Omega microplate reader (BMG Labtech) in 96-well, round-bottom plates (Corning Costar), 300- μ L reaction volumes.

Availability of data and material. Developed genome-scale model (xls) is available on the web-site: <http://sci.sdsu.edu/kalyuzhlab/>.

References

- Shindell, D. *et al.* Simultaneously mitigating near-term climate change and improving human health and food security. *Science* **335**, 183–189 (2012).
- Schaefer, H. *et al.* A 21st-century shift from fossil-fuel to biogenic methane emissions indicated by ¹³CH₄. *Science* **352**, 80–84 (2016).
- Strong, P. J., Xie, S. & Clarke, W. P. Methane as a resource: can the methanotrophs add value? *Env. Sci. Tech.* **49**, 4001–4018 (2015).
- Haynes, C. A. & Gonzalez, R. Rethinking biological activation of methane and conversion to liquid fuels. *Nat. Chem. Biol.* **10**, 331–339 (2014).
- Conrado, R. J. & Gonzalez, R. Envisioning the bioconversion of methane to liquid fuels. *Science* **343**, 621–623 (2014).
- Strong, P. J., Kalyuzhnaya, M., Silverman, J. & Clarke, W. P. A methanotroph-based biorefinery: Potential scenarios for generating multiple products from a single fermentation. *Bioresour. Technol.* **215**, 314–323 (2016).
- Henard, C. A. *et al.* Bioconversion of methane to lactate by an obligate methanotrophic bacterium. *Sci. Rep.* **6**, 21585 (2016).
- Soo, V. W. *et al.* Reversing methanogenesis to capture methane for liquid biofuel precursors. *Microb. Cell Fact.* **15**, 11 (2016).
- Demidenko, A., Akberdin, I. R., Allemann, M., Allen, E. E. & Kalyuzhnaya, M. G. Fatty acid biosynthesis pathways in *Methylomicrobium buryatense* 5G (B1). *Front. Microbiol.* **7**, 2167 (2017).
- Anthony, C. *The Biochemistry of Methylotrophs*. (Academic Press, London, 1982).
- Trotsenko, Y. A. & Murrell, J. C. Metabolic Aspects of Aerobic Obligate Methanotrophy. *Adv. Appl. Microbiol.* **63**, 183–229 (2008).
- Chistoserdova, L. Modularity of methylotrophy, revisited. *Env. Microbiol.* **13**, 2603–2622 (2011).

13. Chistoserdova, L., Kalyuzhnaya, M. G. & Lidstrom, M. E. The expanding world of methylotrophic metabolism. *Ann. Rev. Microbiol.* **63**, 477–499 (2009).
14. Kalyuzhnaya, M. G. *et al.* Reclassification and emended description of halo (alkali) philic and halo (alkali) tolerant methanotrophs of genera *Methylomicrobium* and *Methylobacter*. *Int. J. Syst. Evol. Microbiol.* **58**, 591–596 (2008).
15. Vuilleumier, S. *et al.* Genome sequence of the haloalkaliphilic methanotrophic bacterium *Methylomicrobium alcaliphilum* 20Z. *J. Bacteriol.* **194**, 551–552 (2012).
16. Kalyuzhnaya, M. G. *et al.* Highly efficient methane biocatalysis revealed in a methanotrophic bacterium. *Nat. Commun.* **4**, 2785 (2013).
17. Keltjens, J. T., Pol, A., Reimann, J. & den Camp, H. J. O. PQQ-dependent methanol dehydrogenases: rare-earth elements make a difference. *Appl. Microbiol. Biotechnol.* **98**, 6163–6183 (2014).
18. Leak, D. J. & Dalton, H. *In vivo* studies of primary alcohols, aldehydes and carboxylic acids as electron donors for the methane mono-oxygenase in a variety of methanotrophs. *Microbiol.* **129**, 3487–3497 (1983).
19. Leak, D. J. & Dalton, H. Growth yields of methanotrophs. *Appl. Microbiol. Biotechnol.* **23**, 470–476 (1986).
20. Semrau, J. D., DiSpirito, A. A. & Yoon, S. Methanotrophs and copper. *FEMS Microbiol. Rev.* **34**, 496–531 (2010).
21. Ward, N. *et al.* Genomic insights into methanotrophy: the complete genome sequence of *Methylococcus capsulatus* (Bath). *PLoS Biol.* **2**, e303 (2004).
22. Smith T. J. & Murrell J. C. Methanotrophy. In *Topics in ecological and environmental microbiology* (Eds. Schmidt, T. M., Schaechter, M.). Academic Press (2012).
23. Matsen, J. B., Yang, S., Stein, L. Y., Beck, D. A. & Kalyuzhnaya, M. G. Global molecular analyses of methane metabolism in methanotrophic Alphaproteobacterium, *Methylosinus trichosporium* OB3b. Part I. Transcriptomic study. *Front. Microbiol.* **7**, 1–13 (2013).
24. De la Torre, A. *et al.* Genome-scale metabolic reconstructions and theoretical investigation of methane conversion in *Methylomicrobium buryatense* strain 5G (B1). *Microb. Cell Fact.* **14**, 188 (2015).
25. Khmelenina, V. N., Kalyuzhnaya, M. G., Starostina, N. G., Suzina, N. E. & Trotsenko, Y. A. Isolation and characterization of halotolerant alkaliphilic methanotrophic bacteria from Tuva soda lakes. *Curr. Microbiol.* **35**, 257–261 (1997).
26. Khmelenina, V. N. *et al.* Osmoadaptation in halophilic and alkaliphilic methanotrophs. *Arch. Microbiol.* **172**, 321–329 (1999).
27. Kalyuzhnaya, M. G. *et al.* Classification of halo (alkali) philic and halo (alkali) tolerant methanotrophs provisionally assigned to the genera *Methylomicrobium* and *Methylobacter* and emended description of the genus *Methylomicrobium*. *Int. J. Syst. Evol. Microbiol.* **58**, 591–596 (2008).
28. Reshetnikov, A. S., Khmelenina, V. N. & Trotsenko, Y. A. Characterization of the ectoine biosynthesis genes of haloalkalotolerant obligate methanotroph *Methylomicrobium alcaliphilum* 20Z. *Arch. Microbiol.* **184**, 286–297 (2006).
29. Khmelenina, V. N., Rozova, O. N. & Trotsenko, Y. A. Characterization of the recombinant pyrophosphate-dependent 6-phosphofructokinases from *Methylomicrobium alcaliphilum* 20Z and *Methylococcus capsulatus* Bath. *Methods Enzymol.* **495**, 1–14 (2011).
30. Rozova, O. N., Khmelenina, V. N., Vuilleumier, S. & Trotsenko, Y. A. Characterization of recombinant pyrophosphate-dependent 6-phosphofructokinase from halotolerant methanotroph *Methylomicrobium alcaliphilum* 20Z. *Res. Microbiol.* **161**, 861–868 (2010).
31. Rozova, O. N., Khmelenina, V. N., Gavletdinova, J. Z., Mustakhimov, I. I. & Trotsenko, Y. A. Acetate kinase—an enzyme of the postulated phosphoketolase pathway in *Methylomicrobium alcaliphilum* 20Z. *Antonie Leeuwenhoek* **108**, 965–974 (2015a).
32. Rozova, O. N., Khmelenina, V. N., Bocharova, K. A., Mustakhimov, I. I. & Trotsenko, Y. A. Role of NAD⁺-Dependent Malate Dehydrogenase in the Metabolism of *Methylomicrobium alcaliphilum* 20Z and *Methylosinus trichosporium* OB3b. *Microorganisms* **3**, 47–59 (2015b).
33. Ojala, D. S., Beck, D. A. & Kalyuzhnaya, M. G. Genetic Systems for Moderately Halo (alkali) philic Bacteria of the Genus *Methylomicrobium*. *Methods Enzymol.* **495**, 99 (2011).
34. Li, X., Roberti, R. & Blobel, G. Structure of an integral membrane sterol reductase from *Methylomicrobium alcaliphilum*. *Nature* **517**, 104–107 (2015).
35. Henard, C. A., Smith, H. K. & Guarnieri, M. T. Phosphoketolase overexpression increases biomass and lipid yield from methane in an obligate methanotrophic biocatalyst. *Metab. Eng.* **41**, 152–158 (2017).
36. Xiong, W., Brune, D. & Vermaas, W. F. The γ -aminobutyric acid shunt contributes to closing the tricarboxylic acid cycle in *Synechocystis* sp. PCC 6803. *Mol. Microbiol.* **93**, 786–796 (2014).
37. Khmelenina, V. N., Kalyuzhnaya, M. G. & Trotsenko, Y. A. Physiological and biochemical properties of a haloalkalotolerant methanotroph. *Mikrobiologia (Moscow)* **66**, 365–370 (1997).
38. Roslev, P. & King, G. M. Aerobic and anaerobic starvation metabolism in methanotrophic bacteria. *Appl. Env. Microbiol.* **61**, 1563–1570 (1995).
39. Varma, A. & Palsson, B. O. Stoichiometric flux balance models quantitatively predict growth and metabolic by-product secretion in wild-type *Escherichia coli* W3110. *Appl. Env. Microbiol.* **60**, 3724–3731 (1994).
40. Gilman, A. *et al.* Oxygen-limited metabolism in the methanotroph *Methylomicrobium buryatense* 5GB1C. *PeerJ* **5**, e3945 (2017).
41. Steinhäuser, D., Fernie, A. R. & Araújo, W. L. Unusual cyanobacterial TCA cycles: not broken just different. *Trends in Plant Sci.* **17**(9), 503–509 (2012).
42. Cuevas, D. A. *et al.* From DNA to FBA: how to build your own genome-scale metabolic model. *Front. Microbiol.* **7**, 907 (2016).
43. Orth, J. D., Thiele, I. & Palsson, B. Ø. What is flux balance analysis? *Nat. Biotechnol.* **28**, 245–248 (2010).
44. Bordbar, A., Monk, J. M., King, Z. A. & Palsson, B. O. Constraint-based models predict metabolic and associated cellular functions. *Nat. Rev. Genet.* **15**(2), 107–120 (2014).
45. King, Z. A. *et al.* BiGG Models: A platform for integrating, standardizing and sharing genome-scale models. *Nucleic Acids Res.* **44**(D1), D515–D522 (2016).
46. Feist, A. M., Scholten, J. C., Palsson, B. Ø., Brockman, F. J. & Ideker, T. Modeling methanogenesis with a genome-scale metabolic reconstruction of *Methanosarcina barkeri*. *Mol. Syst. Biol.* **2** (2006).
47. Schellenberger, J. *et al.* Quantitative prediction of cellular metabolism with constraint-based models: the COBRA Toolbox2. *Nat. Protoc.* **6**, 1290–1307 (2011).
48. King, Z. A. *et al.* Escher: a web application for building, sharing, and embedding data-rich visualizations of biological pathways. *PLoS Comput. Biol.* **11**, e1004321 (2015).
49. Seifter, S., Dayton, S., Novic, B. & Muntwyler, E. The estimation of glycogen with the anthrone reagent. *Arch Biochem* **25**, 191–200 (1950).
50. Riis, V., Maskow, T. & Babel, W. Highly sensitive determination of ectoine and other compatible solutes by anion-exchange chromatography and pulsed amperometric detection. *Anal. Bioanal. Chem.* **377**, 203–207 (2003).
51. Albalasmeh, A. A., Berhe, A. A. & Ghezzehei, T. A. A new method for rapid determination of carbohydrate and total carbon concentrations using UV spectrophotometry. *Carbohydr. Polym.* **97**, 253–261 (2013).
52. Long, T. *et al.* Whole-genome sequencing identifies common-to-rare variants associated with human blood metabolites. *Nat. Genet.* **49**, 568–578 (2017).
53. Welch, B. L. The significance of the difference between two means when the population variances are unequal. *Biometrika* **29**, 350–362 (1938).
54. Jolliffe, I. *Principal component analysis*. John Wiley & Sons, Ltd. (2002).

55. Lehman, A., O'Rourke, N., Hatcher, L. & Stepanski, E. JMP for basic univariate and multivariate statistics. *SAS Institute Inc. Cary NC*, **481** (2005).
56. Brown, J. P. & Perham, R. N. Selective inactivation of the transacylase components of the 2-oxo acid dehydrogenase multienzyme complexes of *Escherichia coli*. *Biochem. J.* **155**, 419–427 (1976).
57. Glenn, K. & Smith, K. S. Allosteric regulation of *Lactobacillus plantarum* xylulose 5-phosphate/fructose 6-phosphate phosphoketolase (Xfp). *J. Bacteriol.* **197**, 1157–1163 (2015).
58. Servinsky, M. D. *et al.* Arabinose is metabolized via a phosphoketolase pathway in *Clostridium acetobutylicum* ATCC 824. *J. Ind. Microbiol. Biotechnol.* **39**, 1859–1867 (2012).
59. Banta, A. B., Wei, J. H. & Welander, P. V. A distinct pathway for tetrahymanol synthesis in bacteria. *Proc. Natl. Acad. Sci. USA* **112**, 13478–13483 (2015).
60. Rush, D. *et al.* The bacteriohopanepolyol inventory of novel aerobic methane oxidising bacteria reveals new biomarker signatures of aerobic methanotrophy in marine systems. *PLoS One* **11**, e0165635 (2016).
61. Khmelina, V. N., Beschastny, A. P., Gayazov, R. R. & Trotsenko, Yu. A. Effect of pyrophosphate on growth and metabolism of *Methylobacterium methanica*. *Mikrobiologiya (Moscow)* **63**, 95–98 (1994).
62. Peyraud, R. *et al.* Genome-scale reconstruction and system level investigation of the metabolic network of *Methylobacterium extorquens* AM1. *BMC Syst. Biol.* **5**, 189 (2011).
63. Ivanova, E. G., Fedorov, D. N., Doronina, N. V. & Trotsenko, Y. A. Production of vitamin B 12 in aerobic methylotrophic bacteria. *Microbiol.* **75**, 494–496 (2006).
64. Kalyuzhnaya, M. G. Haloalkaliphilic methanotrophs: isolation and characterization. *PhD thesis. Pushchino* (2000).
65. But, S. Y. *et al.* Sucrose metabolism in halotolerant methanotroph *Methylomicrobium alcaliphilum* 20Z. *Archiv. Microbiol.* **197**, 471–480 (2015).
66. But, S. Y., Egorova, S. V., Khmelina, V. N. & Trotsenko, Y. A. Biochemical properties and phylogeny of hydroxypyruvate reductases from methanotrophic bacteria with different c1-assimilation pathways. *Biochem. (Moscow)* **82**, 1295–1303 (2017).
67. Mustakhimov, I. I. *et al.* The properties and potential metabolic role of glucokinase in halotolerant obligate methanotroph *Methylomicrobium alcaliphilum* 20Z. *Antonie Leeuwenhoek* **110**, 375–386 (2017).
68. Rozova, O. N. *et al.* Characterization of two recombinant 3-hexulose-6-phosphate synthases from the halotolerant obligate methanotroph *Methylomicrobium alcaliphilum* 20Z. *Biochem. (Moscow)* **82**, 176–185 (2017).
69. But, S. Y., Rozova, O. N., Khmelina, V. N., Reshetnikov, A. S. & Trotsenko, Y. A. Properties of recombinant ATP-dependent fructokinase from the halotolerant methanotroph *Methylomicrobium alcaliphilum* 20Z. *Biochem (Moscow)* **77**, 372 (2012).

Acknowledgements

The study was financially supported by DOE under FOA DE-FOA-0001085 and by NSF-CBET award 1605031.

Author Contributions

IRA reconstructed the genome-scale models and performed statistical comparison of metabolite profiling data with predicted flux ratios. MGK, MT and RH conducted cultivation experiments. ND and DA carried out non-targeted biochemical analyses. MG and CH carried out enzymatic studies. MGK designed and coordinated the study. IRA and MGK analyzed data and wrote the manuscript. All authors read and approved the final manuscript.

Additional Information

Supplementary information accompanies this paper at <https://doi.org/10.1038/s41598-018-20574-z>.

Competing Interests: The authors declare no competing interests.

Publisher's note: Springer Nature remains neutral with regard to jurisdictional claims in published maps and institutional affiliations.



Open Access This article is licensed under a Creative Commons Attribution 4.0 International License, which permits use, sharing, adaptation, distribution and reproduction in any medium or format, as long as you give appropriate credit to the original author(s) and the source, provide a link to the Creative Commons license, and indicate if changes were made. The images or other third party material in this article are included in the article's Creative Commons license, unless indicated otherwise in a credit line to the material. If material is not included in the article's Creative Commons license and your intended use is not permitted by statutory regulation or exceeds the permitted use, you will need to obtain permission directly from the copyright holder. To view a copy of this license, visit <http://creativecommons.org/licenses/by/4.0/>.

© The Author(s) 2018